Volume 6 | Number 1 | January 2019

INORGANIC CHEMISTRY

FRONTIERS

CCS CHINESE CHEMICAL SOCIETY

rsc.li/frontiers-inorganic
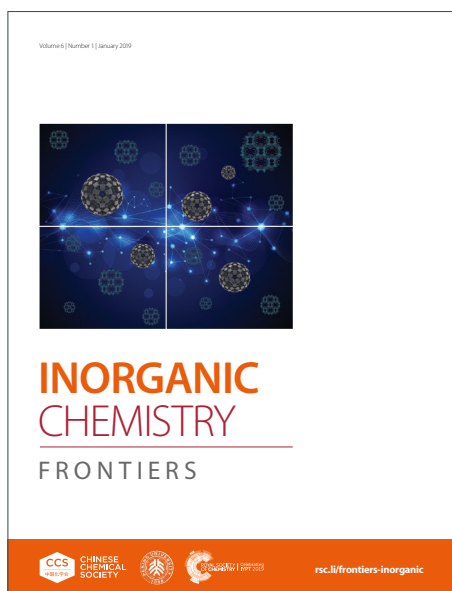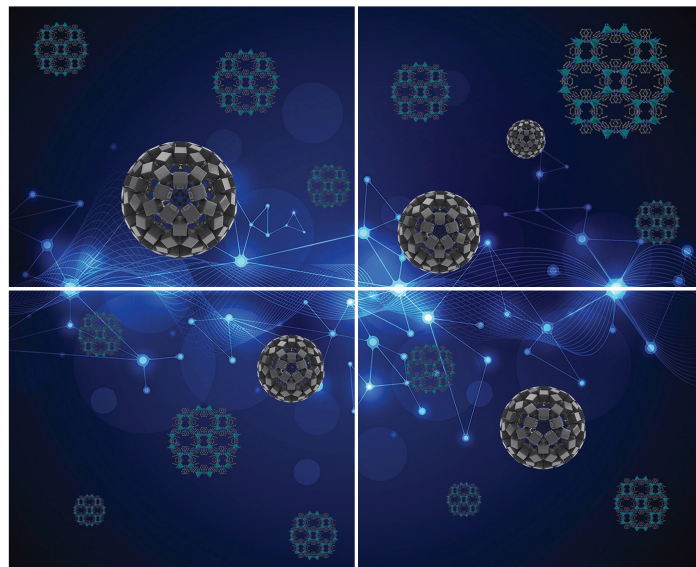
This is an Accepted Manuscript, which has been through the Royal Society of Chemistry peer review process and has been accepted for publication.

Accepted Manuscripts are published online shortly after acceptance, before technical editing, formatting and proof reading. Using this free service, authors can make their results available to the community, in citable form, before we publish the edited article. We will replace this Accepted Manuscript with the edited and formatted Advance Article as soon as it is available.

You can find more information about Accepted Manuscripts in the Information for Authors.

CCS CHINESE CHEMICAL SOCIETY

PEKING UNIVERSITY 1898

ROYAL SOCIETY OF CHEMISTRY

rsc.li/frontiers-inorganic

Confined Replacement Synthesis of SnSe Nanoplates in N-Doped Hollow Carbon Nanocages for High-Performance Sodium-Ion Batteries

Xiang Hu,[b] Xuhui Yang,[d] Yangjie Liu,[b,c] Min Qiu,[b] Zhidong Tian,[b] Yao Guo,[b] Jun Yuan,[b,c] Yichun Ding,[a,b] Hongbing Zhan,*[a,c] Zhenhai Wen*[a,b]

a. Fujian Science & Technology Innovation Laboratory for Optoelectronic Information of China, Fuzhou, Fujian 350108, China.

b. CAS Key Laboratory of Design and Assembly of Functional Nanostructures, and Fujian Provincial Key Laboratory of Nanomaterials, Fujian Institute of Research on the Structure of Matter, Chinese Academy of Sciences, Fuzhou, Fujian 350002, China.

c. College of Materials Science and Engineering, Fuzhou University, Fuzhou, Fujian 350108, China

d. College of Environmental and Resource Sciences, Fujian Normal University, Fuzhou, Fujian 350007, China

*Corresponding author.

Email address: hbzhan@fzu.edu.cn, wen@fjirsm.ac.cn

Abstract

Transition metal selenides are regarded as promising alternatives for Sodium-ion batteries (SIBs) owing to the high theoretical capacity based on conversion reaction. However, the poor electrical conductivity, sluggish reaction kinetics and drastic volume change during cycling severely restrict their practical applications. Herein, we report a facile confined replacement strategy for the synthesis of a yolk-shell nanoarchitecture composed of SnSe nanoplates encapsulated into N-doped hollow carbon nanocages (SnSe@N-HCNs) via strongly C-Se and Sn-C bonding. The favorable yolk-shell structure combined with the strong interface coupling by chemical bonds not only effectively buffer the large volume expansion of SnSe during cycling, but also greatly promote the rapid electron/ion transfer, enabling remarkable pseudocapacitive Na^+ ion storage and high-power capability. As a result, the SnSe@N-HCNs anode exhibits a large reversible capacity of 516 mAh g^{-1} at 0.2 A g^{-1}, exceptional high-rate capability (313 mAh g^{-1} at 10 A g^{-1}) and long-term cycling stability over 1000 cycles. Impressively, when coupled with a hollow $Na_3V_2(PO_4)_3$@C cathode in a sodium-ion full cell, it delivers a high energy density of 177 Wh kg^{-1} at power density of 1200 W kg^{-1} based on the total mass of active materials. The present work offers a new dimension in material design for high performance energy storage devices.

Keywords: Sodium-ion batteries, anode, replacement strategy, SnSe, yolk-shell nanoarchitecture.

1. Introduction

The development and utilization of advanced energy storage devices with high energy density have become urgent priorities to satisfy the need for power sources in future large-scale energy storage applications.[1-3] Sodium ion batteries (SIBs), as a promising substitute for lithium-ion batteries (LIBs), have attracted extensive interest owing to their overwhelming advantages of large reserves and low cost of sodium resources.[4, 5] Substantial efforts have been devoted to explore appropriate anode materials for sodium storage, among which metal selenides (M_xSe_y, M = Fe, Co, Ni, Cu, Zn, Sb, Sn, etc.) have come into the spotlight because of their high theoretical capacity and moderate reaction platform.[6] Unfortunately, most of them suffer from drastic volume expansion, severe particle aggregation and poor electric conductivity during Na^+ insertion/extraction processes, leading to sluggish kinetics, inferior rate capability and fast capacity fading.

To develop advanced M_xSe_y materials for SIBs to host the structural distortion, researchers have focused on the nanostructure design and decoration with carbon species.[7-9] It has indeed been demonstrated that the nanostructured active material can effectively release of the internal mechanical stress and relieve electrode the pulverization problem. Meanwhile, combining with a conductive carbon skeleton can not only enhance their electrical conductivity but also restrict the agglomeration of active particles. However, these nanocomposite anodes usually suffer from the detachment of M_xSe_y from carbon matrix and then the M_xSe_y is directly contact the electrolyte after long-term cycling, leading to grievous side reactions at the interface between the M_xSe_y and electrolyte, and formation of a very thick solid electrolyte interphase (SEI) layer.[10, 11] This is largely due to the weak physical interactions between the polar active materials and nonpolar carbon, and the inevitable volume expansion upon cycling. To solve this critical problem, rational designs in composition and structure should be synchronously executed to strengthen the stability of carbon-containing M_xSe_y nanostructured composites.

Hollow nanostructured materials with well-defined cavities have been reported to show significant advantages in Na^+ storage.[12, 13] The hollow internal reserved void can serve as a buffering zone buffer the large strain caused by the repeated Na^+ insertion/extraction, and the permeable nano-shells can facilitate the transport of electrons/Na^+ and provide a large contact area for complete infiltration of electrolyte. Nevertheless, such simple hollow structure would inevitably lead to a low packing density, which greatly sacrificed their volumetric energy and power densities.[14, 15] To make better utilization of the inner hollow cavity, construction of yolk-shell nanostructure has been proven an effective strategy. Because the energy density of the SIBs can be enhanced by increasing the weight fraction of the electrochemical active core component. However, most of the reported yolk-shell structure usually require a template and operate at a relatively high temperature, followed by selective etching or dissolution the internal sacrificial template, which tend to suffer from high costs, multistep synthetic process, as well as serious environment pollutions.[16-21] Moreover, the hollow shell was likely collapsed during template removal process, which impede the application of the approach. Therefore, it is highly expected but challenging to develop an effective strategy for fabricating yolk-shell structured M_xSe_y nanomaterials.

Herein, we present a facile replacement synthesis route to confine SnSe nanoplates in metal-organic frameworks (MOFs) derived N-doped hollow carbon nanocages (SnSe@N-HCNs). The in situ confined replacement reaction for the formation of yolk-shell structured SnSe@N-HCNs nanocomposite can not only enable strong chemical bonding interactions by C-Se and Sn-C bonds between the interfaces of the SnSe core and external N-doped carbon shell, but also mitigate the volume swelling with SnSe nanoplates agglomeration upon cycling simultaneously, resulting in fast electron/Na^+ transport kinetics and enhanced structural stability. As expected, the strengthened synergistic function features endow the SnSe@N-HCNs electrode with high sodium storage capacity, excellent rate capability and long-term cycling stability when used as an anode in SIBs.

2. Results and discussion

The complete synthesis route of the SnSe@N-HCNs nanocomposite is illustrated in Figure 1a. First, the well-organized ZIF-8 (zeolitic imidazolate framework-8) polyhedrons with a size of around 200 nm were synthesized by a facile solution-based method (Figure S1). After surface coating with polydopamine (PDA) and subsequent selenylation processes, the N-doped carbon-coated ZnSe (ZnSe@NC) are obtained and studied by Field-emission scanning electron microscopy (FESEM) and Transmission electron microscope (TEM) imaging analysis. As shown in Figure S2, the sample still keeps evenly distributed after dopamine polymerization. Moreover, the uniform polyhedron morphology of ZnSe@NC can be further maintained superbly even after high-temperature selenylation reaction (Figure 1b-1c), suggesting the robust structural stability of the porous carbon skeleton. In particular, some mesopores and hollow internal cavity of the ZnSe@NC are clearly observed, revealing a nanocage structure property. Meanwhile, the tiny ZnSe nanoparticles are confined in the hollow cavity of N-doped carbon shell to form a yolk-shell nanoarchitecture during this process. The high-resolution TEM (HRTEM) image exhibits clear lattice spacing of 0.32 nm, corresponding to the (011) plane of ZnSe (Figure 1d).[22]

The ZnSe@NC can be transformed into SnSe@N-HCNs via a facile cation-exchange method during the hydrothermal process. Due to the lower solubility constant of SnSe (K_{sp} =3.98×10^{-39}) than ZnSe (K_{sp} =3.6×10^{-26}), the zinc cations in the ZnSe can be replaced by Sn cations to form SnSe species that were in situ confined in the N-doped carbon nanocage framework forming SnSe@N-HCNs. The low-magnification FESEM images clearly illustrate that the monodispersed nanocage structure of SnSe@N-HCNs is well maintained after the displacement reaction (Figure 1e). Interestingly, the ZnSe nanoparticles are transformed into SnSe nanoplates morphology and fully encapsulated in each carbon nanocage, as verified in the high-magnification FESEM and TEM images (Figure 1f-1h). The representative HRTEM image reveals the multilayered structure with an interplanar distance of 0.58 nm, corresponding to the

d-spacing of (002) plane of orthorhombic SnSe (Figure 1i).[23, 24] The well-defined yolk-shell structure of SnSe@N-HCNs nanocages is further supported by the high-angle annular darkfield scanning TEM (HADDF-STEM) image and corresponding energy-dispersive X-ray spectrum (EDX) elemental mappings (Figure 1j-1n). It can be clearly seen that the homogeneous distribution of Sn and Se elements concentrated around the central core of the N-doped carbon nanocage, confirming the presence of SnSe core in the SnSe@N-HCNs. Moreover, the atomic ratio of Sn:Se in SnSe@N-HCNs is calculated to be 16.2:15.1 according to the EDX analysis, which is close to the stoichiometric ratio of SnSe (Figure S3). In comparison, the SnSe@NC sample was also prepared through a facile solvothermal along with high-temperature calcination method, which displays irregular nanoplates morphology (Figure S4a-d). The HRTEM image reveals that the SnSe is tightly coated by a uniform amorphous carbon layer derived by the PDA decompose (Figure S4e). The weight fraction of carbon in the SnSe@N-HCNs and SnSe@NC composite is determined by thermogravimetric analysis (TGA) to be about 15 wt% and 9 wt%, respectively (Figure S5).

For further proving that these yolk-shell ZnSe@NC were transformed into yolk-shell SnSe@N-HCNs, XRD measurements were performed. As shown in Figure2a, three strong peaks centered at 27.2°, 45.2°, and 53.6° can be indexed to (111), (220), and (311) plane of ZnSe (JCPDS No. 37-1463).[9, 25] Then for SnSe@N-HCNs sample, those peaks belong to ZnSe have been disappeared and the peaks corresponding to SnSe emerged (JCPDS No. 48-1224), confirming the full conversion process from ZnSe to SnSe in the displacement reaction. The Raman spectra displays two obvious peaks located at around 1348 cm^{-1} and 1580 cm^{-1} attributed to the disordered (D band) and graphitic (G band) of carbon shell structure (Figure 2b).[26, 27] The peak intensity ratio of the I_D/I_G is 1.12, suggesting that the degree of graphitic ordering in SnSe@N-HCNs composite is low. In addition, the G band and the D band can be fitted into four peaks by utilizing Gaussian numerical simulation.[28, 29] The peaks at around 1282 and 1578 cm^{-1} (peak 1 and 3) are relevant to sp3-type carbon (amorphous carbon and the defects), while

6

the other two peaks at about 1353 and 1614 cm^{-1} (peak 2 and 4) are correlated to sp2-type carbon (graphitized carbon). The fitted A_{sp3}/A_{sp2} value (the integrated area of sp3 to sp2) is 1.06, further revealing that heteroatom N doping can induce abundant edge defects structures in the carbon matrix of SnSe@N-HCNs. The Brunauer-Emmett-Teller (BET) results show that the specific surface area of SnSe@NC is only 34.7 m^2 g^{-1}. In comparison, the SnSe@N-HCNs has much enlarged surface areas of 126.5 m^2 g^{-1} and their pore size distributions are confirmed a porous structure consist of mesoporous and macropore according to the Barrett-Joyner-Halenda (BJH) results (Figure 2c). The large surface area and porous structure of SnSe@N-HCNs can offer abundant energy storage sites and diffusion channels for Na$^+$ ion, contributing to sufficient contact between the active material and electrolyte.

The surface compositions and valence states of the samples were investigated by X-ray photoelectron spectroscopy (XPS). The full spectrum of SnSe@N-HCNs shows that the signals of C, N, Sn, Se were observed, but the Zn invisible, further confirming that the Zn has been completely replaced by Sn element (Figure S6). The result show that the atomic percentage ratio of Se and Sn is calculated to be about 1:1.04, an ideal chemical stoichiometry of SnSe. The C 1s spectrum of SnSe@N-HCNs shown in Figure 2d exhibits four peaks at 284.6, 285.3, 285.8, and 286.6 eV, corresponding to C=C, C-N, C-O and C=O bonds, respectively.[30, 31] More importantly, the formation of C-Sn (283.7 eV) and C-Se (287.8 eV) bonds could be demonstrated,[23, 33] suggesting the strong chemical bonding interaction at the interface between the SnSe core and the external carbon matrix, which could improve the conductivity and strengthen the structural stability of SnSe@N-HCNs composite. The N 1s XPS spectrum of SnSe@N-HCNs can be fitted into three peaks at 397.8, 400.2, and 403.4 eV, which are normally indexed to pyridinic-N, pyrrolic-N and graphitic-N, respectively (Figure S7).[31] For the Sn 3d XPS spectra (Figure 2e), two spin-orbit doublets at 487.1 and 495.5 eV correspond to the Sn 3d$_{5/2}$ and Sn 3d$_{3/2}$ of Sn^{2+} ions, respectively.[34, 35] In addition, the shoulder peaks at 485.6 and 494.1 eV of the SnSe@N-HCNs can be attributed to Sn-C bonds.[36] The high-resolution XPS

7

spectrum of Se 3d is shown in Figure 2f. Two typical peaks at 54.6 and 55.5 eV for the SnSe@N-HCNs are observed, corresponding to the Se $3d_{5/2}$ and Se $3d_{3/2}$ of Se^{2-}, respectively.[37] In the comparison of SnSe@NC, the Se $3d_{5/2}$ and Se $3d_{3/2}$ of SnSe@N-HCNs have a shift into higher binder energy, which is probably attributed to the enhancement of electronic coupling between SnSe and carbon matrix. The other peak of Se 3d at 57.4 eV is fitted to C-Se bond,[38, 39] further demonstrating the successful doping of Se species in the carbon matrix of SnSe@N-HCNs. To theoretically elucidate the chemical bonding in SnSe@N-HCNs, density functional theory (DFT) calculations were conducted by using the Quantum Espresso (Figure S8). The configuration models of SnSe@N-HCNs and SnSe/C were optimized and the corresponding binding energy (ΔE) were calculated. One can see that the ΔE of SnSe@N-HCNs (-2.26 eV) is lower than that of SnSe@C (-1.27 eV), further demonstrating the strong chemical bonding between SnSe and N-doped carbon nanocage framework.

The Na^+ storage properties of the yolk-shell structure of SnSe@N-HCNs nanocages was initially evaluated in a sodium-ion half-cell using Na metal as the working electrode and counter electrode. Figure 3a presents the initial three cyclic voltammetry (CV) curves of the SnSe@N-HCNs electrode at 0.1 mV s^{-1} in a voltage range of 0.01-2.5 V. During the initial cathodic scan process, the weak and broad reduction peaks ranging from 1.5 to 1.0 V is observed, which can be attributed to the intercalation of Na^+ into the SnSe to generate Na_xSnSe intermediate.[23] The sharp and prominent peak centered at 0.71 V can be assigned to the conversion reaction from Na_xSnSe to Na_2Se and metallic Sn, along with the irreversible decomposition of the electrolyte to construct solid electrolyte interface (SEI) film.[40, 41] In addition, a small peak at around 0.2 V can be identified, corresponding to the multistep alloying processes between metallic Sn and Na to form the Na_xSn alloy.[42] In the corresponding anodic scans process, the oxidation peaks at 0.26, 0.71, 1.09, 1.35 and 1.63 eV can be attributed to the step-by-step dealloying reactions and reverse conversion process.[43] From the second cycle onward, the oxidation and reduction peaks of SnSe@N-HCNs are highly coincident compared with that of the SnSe@NC electrode,

suggesting that the SnSe@N-HCNs has batter electrochemical reversibility (Figure S9a). Moreover, the SnSe@N-HCNs possesses larger CV curve area than SnSe@NC (Figure S9b), implying a higher Na$^+$ storage capacity.

The galvanostatic charge and discharge profiles of SnSe@N-HCNs at a current density of 0.2 A g^{-1} are shown in Figure 3b. The voltage plateau features are consistent with the redox peaks observed in the CV curves. The discharge and charge capacities of the first cycle are 896 and 673 mAh g^{-1}, respectively, corresponding to a coulombic efficiency of 75.1 %. The decrease in the initial charge capacity may come from the irreversible electrolyte degradation and the formation of the SEI films. Figure 3c compares the cyclic behaviors of the SnSe@N-HCNs and SnSe@NC at a current density of 0.2 A g^{-1}. The reversible capacity of the SnSe@N-HCNs electrode is around 572 mAh g^{-1} in the second cycle. After 200 cycles, the SnSe@N-HCNs electrode still maintains a high reversible capacity of 516 mAh g^{-1}, corresponding to a high-capacity retention of 90.2%. In contrast, the SnSe@NC electrode delivers a capacity of 513 mAh g^{-1} in the second cycle and shows gradually decreased reversible specific capacities to only 180 mAh g^{-1} with a capacity retention of 35.1% after 200 cycles. To unravel the structural stability of SnSe@N-HCNs, ex situ TEM measurements were conducted. As shown in Figure S10a, the well-defined yolk-shell nanocages structure is observed when the cell discharges to 1.5 V, indicating only the Na intercalation happened in layered SnSe nanoplates. Further fully sodiation to 0.01 V, the SnSe nanoplates experienced volume expansion owing to the conversion reaction but still confined in the N-doped carbon nanocages (Figure S10b). After the fully desodiation to 2.5 V, one can clearly observe the SnSe nanoplates again and the ratio of Sn to Se closed to 1:1, suggesting that the SnSe@N-HCNs possesses an outstanding structure stability during the sodiation/desodiation process (Figure S10c, d). Moreover, the yolk-shell of SnSe@N-HCNs nanocages morphology is still well maintained without obvious destruction while the SnSe@NC electrode are completely pulverized (Figure S11), indicating that the void space in the SnSe@N-HCNs coupled with the strong chemical bonding interactions can

effectively buffer the mechanical stress caused by the volume change of SnSe during cycling and thus strengthen the structural stability.

The yolk-shell nanostructured SnSe@N-HCNs also has higher rate capability than SnSe@NC, as shown in Figure 3d. The average reversible capacities of the SnSe@N-HCNs are 610, 567, 541, 505, 457, 388, 313 mAh g^{-1} at the current densities of 0.1, 0.2, 0.5, 1, 2, 5 and 10 A g^{-1}. In contrast, the SnSe@NC exhibits a sharp capacity decrease in the current density range of 0.1-5 A g^{-1} and near zero at high current density of 10 A g^{-1}. Furthermore, as the current density returns to 0.1 A g^{-1}, the SnSe@N-HCNs quickly returns to 617 mAh g^{-1}, indicating high electrochemical stability. Figure 3e summarizes the capacity retention rate relative to the reversible capacity at 0.1 A g^{-1} for the SnSe@N-HCNs and SnSe@NC at different current densities. The results indicate that the SnSe@N-HCNs can hold a high-capacity retention rate of 51.3% even with 100-fold increase of current density, demonstrating the superior rate performance. The excellent rate capability of the SnSe@N-HCNs electrode can be further confirmed by the low polarized discharge-charge voltage curves at different current densities (Figure 3f). When compared with the previous reported tin selenide-based anodes materials for SIBs, the present SnSe@N-HCNs electrode displays apparent superiority in rate capability (Figure 3g).[23, 32, 36, 37, 44-48] Moreover, the SnSe@N-HCNs electrode also exhibits superior long-term cycling stability. As shown in Figure 3h, although an obvious capacity decay in the initial cycles can be observed owing to the formation of a stable SEI film, the SnSe@N-HCNs electrode shows a high capacity of 425 mAh g^{-1} over 1000 cycles with close to 100% coulombic efficiency at 1 A g^{-1}, which is superior to most of the reported Tin-based compound electrodes (Table S1) However, the capacity of SnSe@NC sharply decayed and almost reach to zero after 1000 cycles at 1 A g^{-1}.

To unravel the origin of the superior Na$^+$ ions storage ability of the SnSe@N-HCNs electrode, kinetic study based on CV measurements and electrochemical impedance spectroscopy (EIS) were conducted. Figure 4a presents the CV curves of the SnSe@N-HCNs electrode at various

scan rates ranging from 0.3 to 1.7 mV s^{-1}. Compared with the SnSe@NC (Figure S12a), the SnSe@N-HCNs display a better-maintained shape of the CV curves with a cathodic and anodic peak separation with stepwise increasing the scan rates, which further explains the good rate ability of the SnSe@N-HCNs. Generally, the power-law relationship between the peak current (i) and the scan rate (v) could be calculated based on the following formulas:[49, 50]

$$i = a v^b \qquad (1)$$

$$\log(i) = b \log(v) + \log(a) \qquad (2)$$

The charge storage mechanism type of electrochemical reaction process is strongly related to the b value. Specifically, the b value of 0.5 indicates a totally diffusion-dominated behavior, whereas the b value of 1.0 represents an ideally surface-controlled capacitive process. Through linear fitting, the calculated b-values at the cathodic and anodic peaks of the SnSe@N-HCNs are 0.793, 0.807, 0.889, and 0.798, respectively, which are significantly greater than that of SnSe@NC electrode, illustrating that the SnSe@N-HCNs electrode is more inclined to surface capacitor behavior and result in a rapid charge storage capability (Figure 4d and S12b). More specifically, the capacitive contribution at a fixed scan rate can be further quantified based on the current (i) measured at a specific potential (V), according to the following equations:[51, 52]

$$i(V) = k_1 v + k_2 v^{1/2} \qquad (3)$$

$$i(V)/v^{1/2} = k_1 v^{1/2} + k_2 \qquad (4)$$

where both k_1 and k_2 are adjustable parameters, $k_1 v$ and $k_2 v^{1/2}$ correspond to the capacitive-controlled and diffusion-dominated process, respectively. For instance, the SnSe@N-HCNs electrode displays 84.4% dominating capacitive contribution (the red region) at 0.9 mV s^{-1} (Figure 4c). In addition, the proportion of capacitive contribution increases with an increasing scanning rate and finally reaches as high as 94.2% at 1.7 mV s^{-1} (Figure 4d), which are clearly higher than the SnSe@NC electrode at each scan rate (Figure S12c, d), further implying a rapid sodium-storage behavior even under high current density. The fast kinetics of SnSe@N-HCNs

electrode is also determined by electrochemical impedance spectroscopy (EIS) results (Figure 4e). The shapes of the plots of the SnSe@N-HCNs and SnSe@NC are similar, with a semicircle in the high-frequency range and a straight line in the low-frequency range. The high-frequency semicircle corresponds to the charge-transfer resistance (R_{ct}), while the low-frequency sloping line represents the Warburg impendence (Z_w) of Na^+ ion diffusion process. According to the EIS equivalent circuit (the inset of Figure 4e), the R_{ct} value of SnSe@N-HCNs (78 Ω) is much lower than that of SnSe@NC (216 Ω), demonstrating the remarkably improved electron transportation in the yolk-shell nanostructured of SnSe@N-HCNs electrode. Additionally, Figure 4f shows the Z'-$\omega^{-1/2}$ ($\omega = 2\pi f$) curves in the low-frequency region, and the lower slope of the SnSe@N-HCNs further proves its faster Na^+ reaction kinetics. The Na ion diffusion coefficient (D_{Na}, cm^2 s^{-1}) can be estimated from the galvanostatic intermittent titration technique (GITT) according to the simplified Fick's second law with the following equation:[53-55]

$$D = \frac{4}{\pi\tau}\left(\frac{m_B V_M}{M_B S}\right)^2\left(\frac{\Delta E_s}{\Delta E_\tau}\right)^2 \qquad (5)$$

where τ and ΔE_τ are the duration of the current pulse and the change of voltage during the current pulse; m_B, M_B (g mol^{-1}), V_M (cm^3 mol^{-1}) and S (cm^2) are the electrode mass, molecular weight, molar volume and the geometric area of active materials. ΔE_s and ΔE_t are the potential changes in the rest and discharge steps after subtracting the IR drop and can be obtained from the GITT curves. As a result, SnSe@N-HCNs electrode exhibits smaller polarization and higher diffusion coefficient during the sodiation/desodiation process (Figure 4g, h and S13), further reflecting its much better sodium storage kinetics.

Based on above results, the reason resulting in the excellent electrochemical performance of the SnSe@N-HCNs is summarized as follows. Firstly, the yolk-shell structure can not only offer large electrode-electrolyte contact area but also offer sufficient buffer space to accommodate the large volume expansion of SnSe during repeated Na^+ ion extraction/insertion

process, rendering robust structure stability and rapid capacitive storage behavior. Secondly, the nanoscale building units of SnSe nanoplates with layered structure can shorten electron/Na^+ ion diffusion pathways and thus accelerate the reaction kinetics. Thirdly, the strong electronic coupling of C-Se and Sn-C bonding between SnSe core and N-doped hollow carbon nanocages shell significantly improve the electrical conductivity and further strengthen the structural stability of the overall electrode, contributing to the wonderful cycling stability and high-rate capability.

To elucidate the practical applications of the SnSe@N-HCNs electrode, full cells were assembled by using $Na_3V_2(PO_4)_3$@C cathode material as counter electrode (Figure 5a). The morphology and phase structure of the $Na_3V_2(PO_4)_3$@C are shown in Figure S14. Specially, the $Na_3V_2(PO_4)_3$@C with a hollow porous microspheres morphology are coated by an uniform carbon layer, which is beneficial to the electrolyte penetration and electron transfer. The electrochemical performance of the hollow $Na_3V_2(PO_4)_3$@C was initially evaluated in half cells and the results are displayed in Figure S15. It exhibits a couple of characteristic charge/discharge plateaus located at 3.41/3.36 V with high reversible specific capacity of 109 mAh g^{-1} at 0.1 A g^{-1}. Moreover, the $Na_3V_2(PO_4)_3$@C delivers an excellent rate capability and long-term cycling stability with high reversible capacity of 82 mAh g^{-1} after 800 cycles at 2 A g^{-1}. Therefore, the weight ratio of the cathode to the anode was set at around 4:1 in the $Na_3V_2(PO_4)_3$@C//SnSe@N-HCNs full cell to balance the capacity between cathode and anode.

Figure 5b reveals the charge/discharge curves of the as-prepared full cell for the first four cycles in the voltage window of 1.0-4.0 V at a current density of 0.5 A g^{-1}. It can be observed that the discharge capacity of the first cycle is 89 mAh g^{-1} (based on the mass of the cathode) with an output voltage plateau at 2.4 V. Therefore, the energy density of the full-cell was calculated to be 177 Wh kg^{-1} (with power density of 1200 W kg^{-1}) based on the total mass of cathode and anode. Meanwhile, the full cell can maintain a specific capacity of 78 mAh g^{-1} after 100 cycles, corresponding to a prominent capacity retention of 87.6%. The full-cell also exhibits

an outstanding rate performance. As shown Figure 5d, it delivers an average reversible capacities of 102, 92, 84, 77, 68, 61, 52 mAh g^{-1} at the current densities of 0.1, 0.2, 0.5, 1, 2, 5 and 8 A g^{-1}, respectively. Moreover, when the current density returns to 0.1 A g^{-1}, the reversible capacity can be recovered to the initial level, indicating the superior electrochemical reversibility and structure stability even under high current density. In addition, the Na$_3$V$_2$(PO$_4$)$_3$@C//SnSe@N-HCNs full cell can easily light up different colors of light-emitting diode (LED) bulbs (inset in Figure 5c), demonstrating the SnSe@N-HCNs has great prospect for practical applications in SIBs.

3. Conclusion

In summary, the yolk-shell structure of SnSe@N-HCNs nanocages were successfully synthesized by a facile replacement reaction during the hydrothermal process. Benefiting from the favorable synergistic effects of strong interface chemical coupling between SnSe nanoplates and N-doped hollow carbon nanocages, the SnSe@N-HCNs possesses excellent structural features with enhanced electric conductivity, fast ion transport channels, reduced volume deformation and remarkable pseudocapacitive Na$^+$ storage behavior. As a result, the SnSe@N-HCNs presents fantastic sodium storage properties in terms of high capacity, good rate capability and long-term cyclability for both sodium-ion half-cell and full-cell. This study may provide a valuable guidance for the design and fabrication of other advanced materials used in various energy storage devices.

Conflicts of interest

There are no conflicts to declare.

References

1. C. Zhao, Q. Wang, Z. Yao, J. Wang, B. Sanchez-Lengeling, F. Ding, X. Qi, Y. Lu, X. Bai, B. Li, H. Li, A. Aspuru-Guzik, X. Huang, C. Delmas, M. Wagemaker, L. Chen and Y. S. Hu, Rational design of layered oxide materials for sodium-ion batteries, *Science*, 2020, **370**, 708-711.

2. J.-N. Zhang, Q. Li, C. Ouyang, X. Yu, M. Ge, X. Huang, E. Hu, C. Ma, S. Li, R. Xiao, W. Yang, Y. Chu, Y. Liu, H. Yu, X.-Q. Yang, X. Huang, L. Chen and H. Li, Trace doping of multiple elements enables stable battery cycling of $LiCoO_2$ at 4.6 V, *Nat. Energy*, 2019, **4**, 594-603.

3. X. Hu, G. Wang, J. Li, J. Huang, Y. Liu, G. Zhong, J. Yuan, H. Zhan and Z. Wen, Significant contribution of single atomic Mn implanted in carbon nanosheets to high-performance sodium-ion hybrid capacitors, *Energy Environ. Sci.*, 2021, **14**, 4564-4573.

4. J. Y. Hwang, S. T. Myung and Y. K. Sun, Sodium-ion batteries: present and future, *Chem. Soc. Rev.*, 2017, **46**, 3529-3614.

5. H. Huang, R. Xu, Y. Feng, S. Zeng, Y. Jiang, H. Wang, W. Luo and Y. Yu, Sodium/potassium-ion batteries: boosting the rate capability and cycle life by combining morphology, defect and structure engineering, *Adv. Mater.*, 2020, **32**, 1904320.

6. Z. Hu, Q. Liu, S. L. Chou and S. X. Dou, Advances and challenges in metal sulfides/selenides for next-generation rechargeable sodium-ion batteries, *Adv. Mater.*, 2017, **29**, 1700606.

7. Y. Li, Y. Xu, Z. Wang, Y. Bai, K. Zhang, R. Dong, Y. Gao, Q. Ni, F. Wu, Y. Liu and C. Wu, Stable carbon-selenium bonds for enhanced performance in tremella-like 2D chalcogenide battery anode, *Adv. Energy Mater.*, 2018, **8**, 1800927.

8. X. J. Xu, J. Liu, J. W. Liu, L. Z. Ouyang, R. Z. Hu, H. Wang, L. C. Yang and M. Zhu, A general metal-organic framework-derived selenidation strategy for in situ carbon-encapsulated metal selenides as high-rate anodes for Na-ion batteries, *Adv. Funct. Mater.*, 2018, **28**, 1707573.

9. X. Y. Li, Z. Y. Han, W. H. Yang, Q. Li, H. S. Li, J. Xu, H. L. Li, B. Liu, H. G. Zhao, S. D. Li, X. Wang and X. L. Wu, 3D ordered porous hybrid of ZnSe/N-doped carbon with anomalously high Na^+ mobility and ultrathin solid electrolyte interphase for sodium-ion batteries, *Adv. Funct. Mater.*, 2021, **31**, 2106194.

10. P. Ge, S. Li, L. Xu, K. Zou, X. Gao, X. Cao, G. Zou, H. Hou and X. Ji, Hierarchical hollow-microsphere metal-selenide@carbon composites with rational surface engineering for advanced sodium storage, *Adv. Energy Mater.*, 2019, **9**, 1803035.

11. J. Chen, Y. Luo, W. Zhang, Y. Qiao, X. Cao, X. Xie, H. Zhou, A. Pan and S. Liang, Tuning interface bridging between $MoSe_2$ and three-dimensional carbon framework by incorporation of MoC intermediate to boost lithium storage capability, *Nano-Micro Lett.*, 2020, **12**, 171.

12. J. Nai and X. W. D. Lou, Hollow structures based on prussian blue and its analogs for electrochemical energy storage and conversion, *Adv. Mater.*, 2019, **31**, 1706825.

13. L. Yu, H. B. Wu and X. W. Lou, Self-Templated Formation of Hollow Structures for Electrochemical Energy Applications, *Acc. Chem. Res.*, 2017, **50**, 293-301.

14. L. Zhang, C. Wang, Y. Dou, N. Cheng, D. Cui, Y. Du, P. Liu, M. Al-Mamun, S. Zhang and H. Zhao, A yolk-shell structured silicon anode with superior conductivity and high tap density for full lithium-ion batteries, *Angew. Chem. Int. Ed.*, 2019, **58**, 8824-8828.

15. Y. Liang, N. Song, Z. Zhang, W. Chen, J. Feng, B. Xi and S. Xiong, Integrating Bi@C nanospheres in porous hard carbon frameworks for ultrafast sodium storage, *Adv. Mater.*, 2022, **34**, 2202673.

16. H. Liu, B. Liu, H. Guo, M. Liang, Y. Zhang, T. Borjigin, X. Yang, L. Wang and X. Sun, N-doped C-encapsulated scale-like yolk-shell frame assembled by expanded planes

few-layer $MoSe_2$ for enhanced performance in sodium-ion batteries, *Nano Energy*, 2018, **51**, 639-648.

17.   J. Song, P. Yan, L. Luo, X. Qi, X. Rong, J. Zheng, B. Xiao, S. Feng, C. Wang, Y.-S. Hu, Y. Lin, V. L. Sprenkle and X. Li, Yolk-shell structured Sb@C anodes for high energy Na-ion batteries, *Nano Energy*, 2017, **40**, 504-511.

18.   S. Y. Lu, T. X. Zhu, H. Wu, Y. K. Wang, J. Li, A. Abdelkaderkh, K. Xi, W. Wang, Y. G. Li, S. J. Ding, G. X. Gao and R. V. Kumarh, Construction of ultrafine ZnSe nanoparticles on/in amorphous carbon hollow nanospheres with high-power-density sodium storage, *Nano Energy*, 2019, **59**, 762-772.

19.   X. C. Ren, Z. G. Ren, Q. W. Li, W. Wen, X. F. Li, Y. Chen, L. Xie, L. Zhang, D. M. Zhu, B. Gao, P. K. Chu and K. F. Huo, Tailored plum pudding-like Co_2P/Sn encapsulated with carbon nanobox shell as superior anode materials for high-performance sodium-ion capacitors, *Adv. Energy Mater.*, 2019, **9**, 1900091.

20.   H. Zhang, X. Huang, O. Noonan, L. Zhou and C. Yu, Tailored yolk-shell Sn@C nanoboxes for high-performance lithium storage, *Adv. Funct. Mater.*, 2017, **27**, 1606023.

21.   S. Wang, Y. Fang, X. Wang and X. W. D. Lou, Hierarchical microboxes constructed by SnS nanoplates coated with nitrogen-doped carbon for efficient sodium storage, *Angew. Chem. Int. Ed.*, 2019, **58**, 760-763.

22.   Y. He, L. Wang, C. Dong, C. Li, X. Ding, Y. Qian and L. Xu, In-situ rooting ZnSe/N-doped hollow carbon architectures as high-rate and long-life anode materials for half/full sodium-ion and potassium-ion batteries, *Energy Storage Mater.*, 2019, **23**, 35-45.

23.   X. Ren, J. Wang, D. Zhu, Q. Li, W. Tian, L. Wang, J. Zhang, L. Miao, P. K. Chu and K. Huo, Sn-C bonding riveted SnSe nanoplates vertically grown on nitrogen-doped carbon nanobelts for high-performance sodium-ion battery anodes, *Nano Energy*, 2018, **54**, 322-330.

24.   S. Yuan, Y. H. Zhu, W. Li, S. Wang, D. Xu, L. Li, Y. Zhang and X. B. Zhang, Surfactant-free aqueous synthesis of pure single-crystalline SnSe nanosheet clusters as anode for high energy-and power-density sodium-ion batteries, *Adv. Mater.*, 2017, **29**, 1602469.

25.   S. Men, H. Zheng, D. Ma, X. Huang and X. Kang, Unraveling the stabilization mechanism of solid electrolyte interface on ZnSe by rGO in sodium ion battery, *J. Energy Chem.*, 2021, **54**, 124-130.

26.   Q. Liu, Y. X. Ji, X. M. Yin, J. W. Li, Y. J. Liu, X. Hu and Z. H. Wen, Magnesiothermic reduction improved route to high-yield synthesis of interconnected porous Si@C networks anode of lithium ions batteries, *Energy Storage Mater.*, 2022, **46**, 384-393.

27.   J. Yuan, M. Qiu, J. X. Chen, X. Hu, Y. Liu, B. Yu, G. Zhong, Z. Weng, H. Zhan and Z. Wen, High mass loading 3D-printed sodium-ion hybrid capacitors, *Adv. Funct. Mater.*, 2022, **32**, 2203732.

28.   Z. Tan, S. Liu, X. Zhang, J. Wei, Y. Liu, L. Hou, C. Yuan, Few-layered V_2C MXene derived 3D V_3S_4 nanocrystal functionalized carbon flakes boosting polysulfide adsorption and catalytic conversion towards Li-S batteries, *J. Mater. Chem. A,* 2022, **10**, 18679.

29.   L. Hou, Z. Chen, Z. Zhao, X. Sun, J. Zhang, C. Yuan, Universal $FeCl_3$-activating strategy for green and scalable fabrication of sustainable biomass-derived hierarchical porous nitrogen-doped carbons for electrochemical supercapacitors, *ACS Appl. Energy Mater.,* 2018, **2**, 548.

30.   X. Hu, Y. Liu, J. Li, G. Wang, J. Chen, G. Zhong, H. Zhan and Z. Wen, Self-assembling of conductive interlayer-expanded WS_2 nanosheets into 3D hollow hierarchical microflower bud hybrids for fast and stable sodium storage, *Adv. Funct. Mater.*, 2019, **30**, 1907677.

31.   Z. Xiang Huang, B. Liu, D. Kong, Y. Wang and H. Ying Yang, $SnSe_2$ quantum dot/rGO composite as high performing lithium anode, *Energy Storage Mater.*, 2018, **10**, 92-101.

32.   J. Hou, Z. Zhu, C. Li, J. Zhang, S. Shen, Z. Yao, T. Liu, W. Li, X. Xia and Y. Yang, Spatially confined synthesis of SnSe spheres encapsulated in N, Se dual-doped carbon networks toward fast and durable sodium storage, *ACS Appl. Mater Interfaces*, 2022, **14**, 4230-4241.

33.   J. Yang, S. Xiao, X. Cui, W. Dai, X. Lian, Z. Hao, Y. Zhao, J.-S. Pan, Y. Zhou, L. Wang and W. Chen, Inorganic-anion-modulated synthesis of 2D nonlayered aluminum-based metal-organic frameworks as carbon precursor for capacitive sodium ion storage, *Energy Storage Mater.*, 2020, **26**, 391-399.

34.   X. Hu, J. Chen, G. Zeng, J. Jia, P. Cai, G. Chai and Z. Wen, Robust 3D macroporous structures with SnS nanoparticles decorating nitrogen-doped carbon nanosheet networks for high performance sodium-ion batteries, *J. Mater. Chem. A*, 2017, **5**, 23460-23470.

35.   D. Chao, B. Ouyang, P. Liang, T. T. T. Huong, G. Jia, H. Huang, X. Xia, R. S. Rawat and H. J. Fan, C-plasma of hierarchical graphene survives SnS bundles for ultrastable and high volumetric Na-ion storage, *Adv. Mater.*, 2018, **30**, 1804833.

36.   M. Wang, A. Peng, H. Xu, Z. Yang, L. Zhang, J. Zhang, H. Yang, J. Chen, Y. Huang and X. Li, Amorphous SnSe quantum dots anchoring on graphene as high performance anodes for battery/capacitor sodium ion storage, *J. Power Sources*, 2020, **469**, 228414.

37.   C. Lu, Z. Z. Li, Z. Xia, H. N. Ci, J. S. Cai, Y. Z. Song, L. H. Yu, W. J. Yin, S. X. Dou, J. Y. Sun and Z. F. Liu, Confining MOF-derived SnSe nanoplatelets in nitrogen-doped graphene cages via direct CVD for durable sodium ion storage, *Nano Res.*, 2019, **12**, 3051-3058.

38.   S. Xiao, Z. Li, J. Liu, Y. Song, T. Li, Y. Xiang, J. S. Chen and Q. Yan, Se-C bonding promoting fast and durable Na$^+$ storage in yolk-shell SnSe$_2$@Se-C, *Small*, 2020, **16**, 2002486.

39.   K. Yang, X. Zhang, K. Song, J. Zhang, C. Liu, L. Mi, Y. Wang and W. Chen, Se-C bond and reversible SEI in facile synthesized SnSe$_2$⊂3D carbon induced stable anode for sodium-ion batteries, *Electrochim. Acta*, 2020, **337**, 135783.

40.   J. Xia, Y. Yuan, H. Yan, J. Liu, Y. Zhang, L. Liu, S. Zhang, W. Li, X. Yang, H. Shu, X. Wang and G. Cao, Electrospun SnSe/C nanofibers as binder-free anode for lithium-ion and sodium-ion batteries, *J. Power Sources*, 2020, **449**, 227559.

41.   X. Yang, R. Zhang, N. Chen, X. Meng, P. Yang, C. Wang, Y. Zhang, Y. Wei, G. Chen and F. Du, Assembly of SnSe nanoparticles confined in graphene for enhanced sodium-ion storage performance, *Chemistry*, 2016, **22**, 1445-1451.

42.   D. Cheng, L. Yang, R. Hu, J. Liu, R. Che, J. Cui, Y. Wu, W. Chen, J. Huang, M. Zhu and Y. J. Zhao, Sn-C and Se-C co-bonding SnSe/few-layered graphene micro-nano structure: route to a densely compacted and durable anode for lithium/sodium-ion batteries, *ACS Appl. Mater. Interfaces*, 2019, **11**, 36685-36696.

43.   Y. Y. Wang, B. H. Hou, Y. N. Wang, H. Y. Lu, J. Z. Guo, Q. L. Ning, J. P. Zhang, C. L. Lu and X. L. Wu, Multiple heterointerfaces boosted de-/sodiation kinetics towards superior Na storage and Na-ion full battery, *J. Mater. Chem. A*, 2018, **6**, 6578-6586.

44.   W. Wang, P. Li, H. Zheng, Q. Liu, F. Lv, J. Wu, H. Wang and S. Guo, Ultrathin layered SnSe nanoplates for low voltage, high-rate, and long-life alkali-ion batteries, *Small*, 2017, **13**, 1702228.

45. T. Wang, D. Legut, Y. Fan, J. Qin, X. Li and Q. Zhang, Building fast diffusion channel by constructing metal sulfide/metal selenide heterostructures for high-performance sodium ion batteries anode, *Nano Lett.*, 2020, **20**, 6199-6205.

46. P. Liu, J. Han, K. Zhu, Z. Dong and L. Jiao, Heterostructure $SnSe_2/ZnSe@PDA$ nanobox for stable and highly efficient sodium-ion storage, *Adv. Energy Mater.*, 2020, **10**, 2000741.

47. H. Chen, Z. Mu, Y. Li, Z. Xia, Y. Yang, F. Lv, J. Zhou, Y. Chao, J. Wang, N. Wang and S. Guo, $SnSe_2$ Nanocrystals coupled with hierarchical porous carbon microspheres for long-life sodium ion battery anode, *Sci. China Mater.*, 2019, **63**, 483-491.

48. F. Zhang, C. Xia, J. Zhu, B. Ahmed, H. Liang, D. B. Velusamy, U. Schwingenschlögl and H. N. Alshareef, $SnSe_2$ 2D anodes for advanced sodium ion batteries, *Adv. Energy Mater.*, 2016, **6**, 1601188.

49. X. L. Cheng, R. W. Shao, D. J. Li, H. Yang, Y. Wu, B. Wang, C. H. Sun, Y. Jiang, Q. B. Zhang and Y. Yu, A self-healing volume variation three-dimensional continuous bulk porous bismuth for ultrafast sodium storage, *Adv. Funct. Mater.*, 2021, **31**, 2011264.

50. Y. Liu, X. Hu, J. Li, G. Zhong, J. Yuan, H. Zhan, Y. Tang and Z. Wen, Carbon-coated $MoS_{1.5}Te_{0.5}$ nanocables for efficient sodium-ion storage in non-aqueous dual-ion batteries, *Nat. Commun.*, 2022, **13**, 663.

51. J. Ma, S. Zheng, L. Chi, Y. Liu, Y. Zhang, K. Wang and Z. S. Wu, 3D printing flexible sodium-ion microbatteries with ultrahigh areal capacity and robust rate capability, *Adv. Mater.*, 2022, **34**, 2205569.

52. B. Wang, J. Li, M. Ye, Y. Zhang, Y. Tang, X. Hu, J. He and C. C. Li, Dual-redox sites guarantee high-capacity sodium storage in two-dimension conjugated metal-organic frameworks, *Adv. Funct. Mater.*, 2022, **32**, 2112072.

53. P. Xiong, P. Bai, A. Li, B. Li, M. Cheng, Y. Chen, S. Huang, Q. Jiang, X. H. Bu and Y. Xu, Bismuth nanoparticle@carbon composite anodes for ultralong cycle life and high-rate sodium-ion batteries, *Adv. Mater.*, 2019, **31**, 1904771.

54. M. Jia, W. Zhang, X. Cai, X. Zhan, L. Hou, C. Yuan, Z. Guo, Re-understanding the galvanostatic intermittent titration technique: Pitfalls in evaluation of diffusion coefficients and rational suggestions. *J. Power Sources,* 2022, **543**, 231843.

55. L. Wang, Y. Ni, K. Lei, H. Dong, S. Tian, F. Li, 3D porous tin created by tuning the redox potential as an advanced electrode for sodium-ion batteries. *ChemSusChem,* 2018, **11**, 3376-3381.
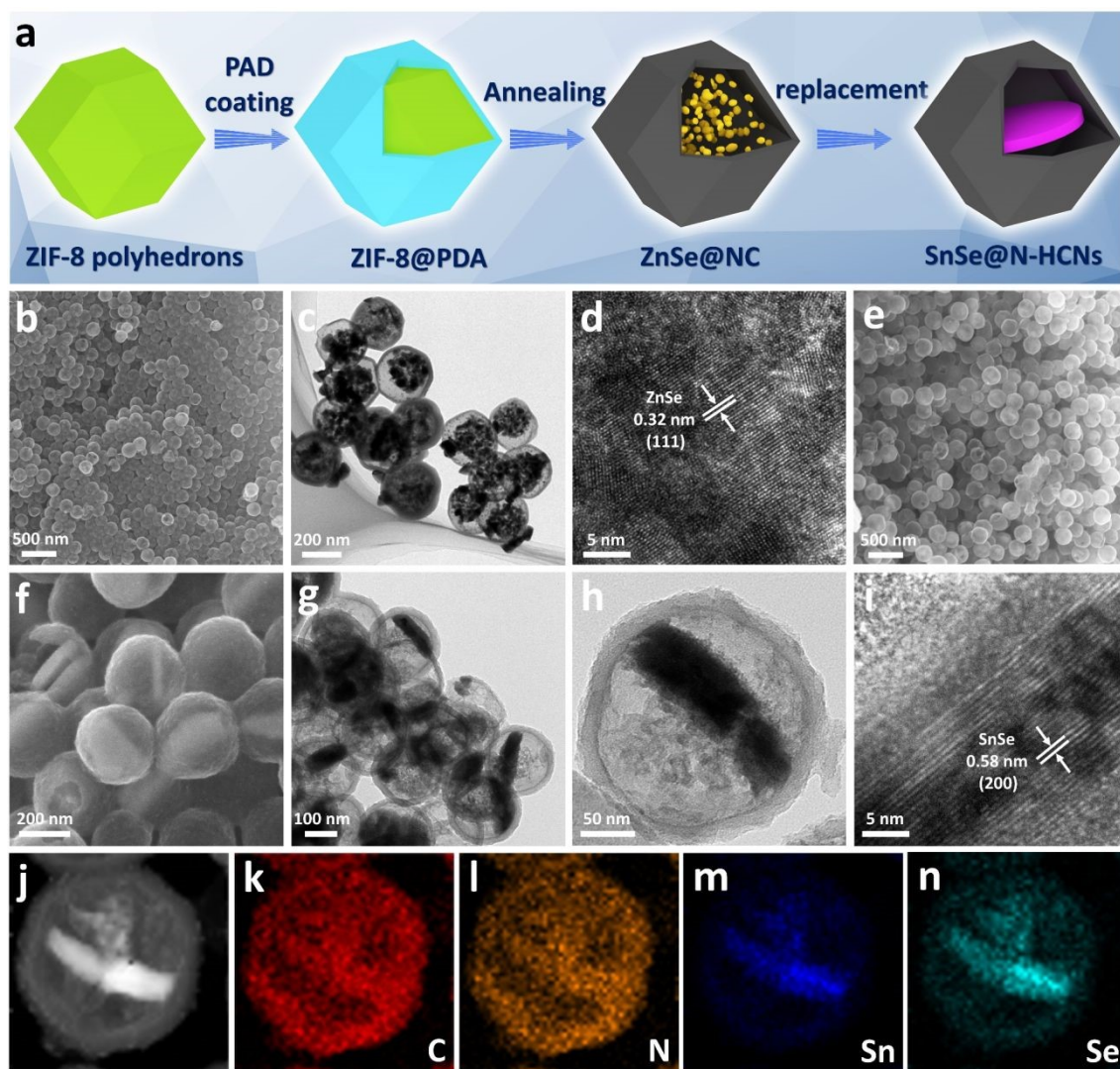
Figure 1. (a) Synthesis process of SnSe@N-HCNs nanocomposite. (b) FESEM image, (c, d) TEM and HRTEM images of ZnSe@NC. (e, f) FESEM images, (g, h) TEM images, (i) HRTEM image, (j) HAADF-STEM image and (k-n) EDS elemental mappings of the SnSe@N-HCNs.
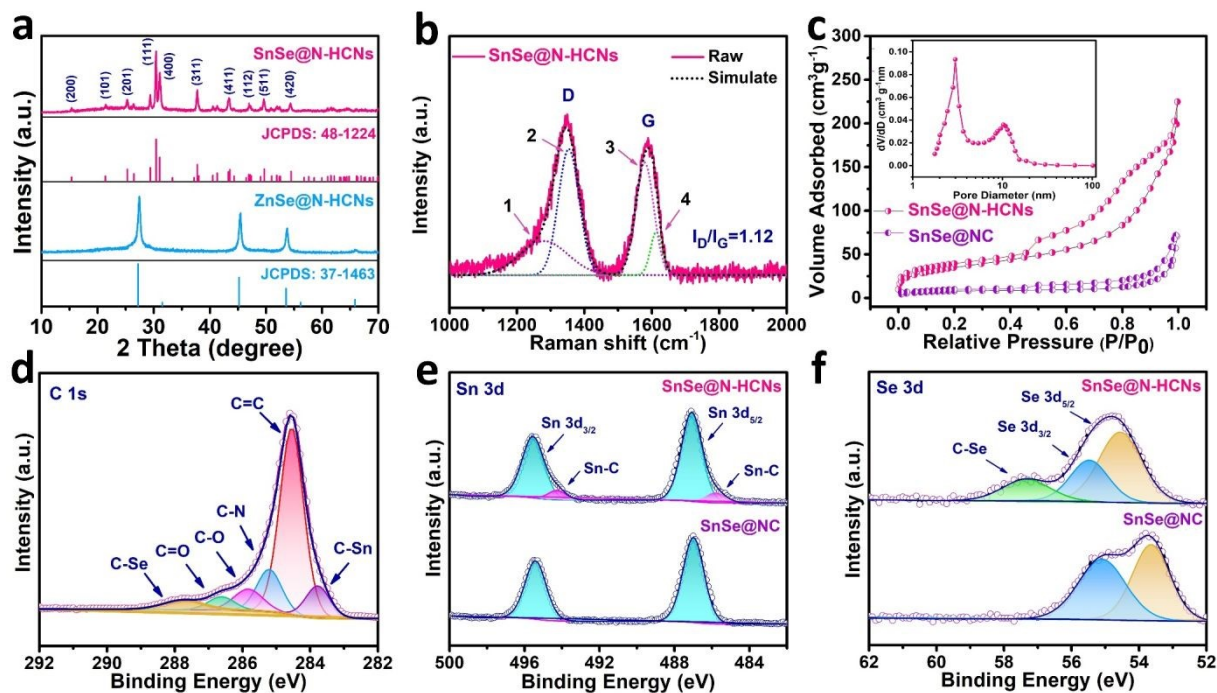
Figure 2. (a) XRD patterns of ZnSe@NC and SnSe@N-HCNs. (b) Raman spectra of SnSe@N-HCNs. (c) Nitrogen adsorption-desorption isothermal curves of SnSe@N-HCNs and SnSe@NC, (inset: pore size distribution of SnSe@N-HCNs). (d) High-resolution XPS spectra of C 1s of SnSe@N-HCNs. High-resolution (e) Sn 3d and (f) Se 3d spectra of SnSe@N-HCNs and SnSe@NC.
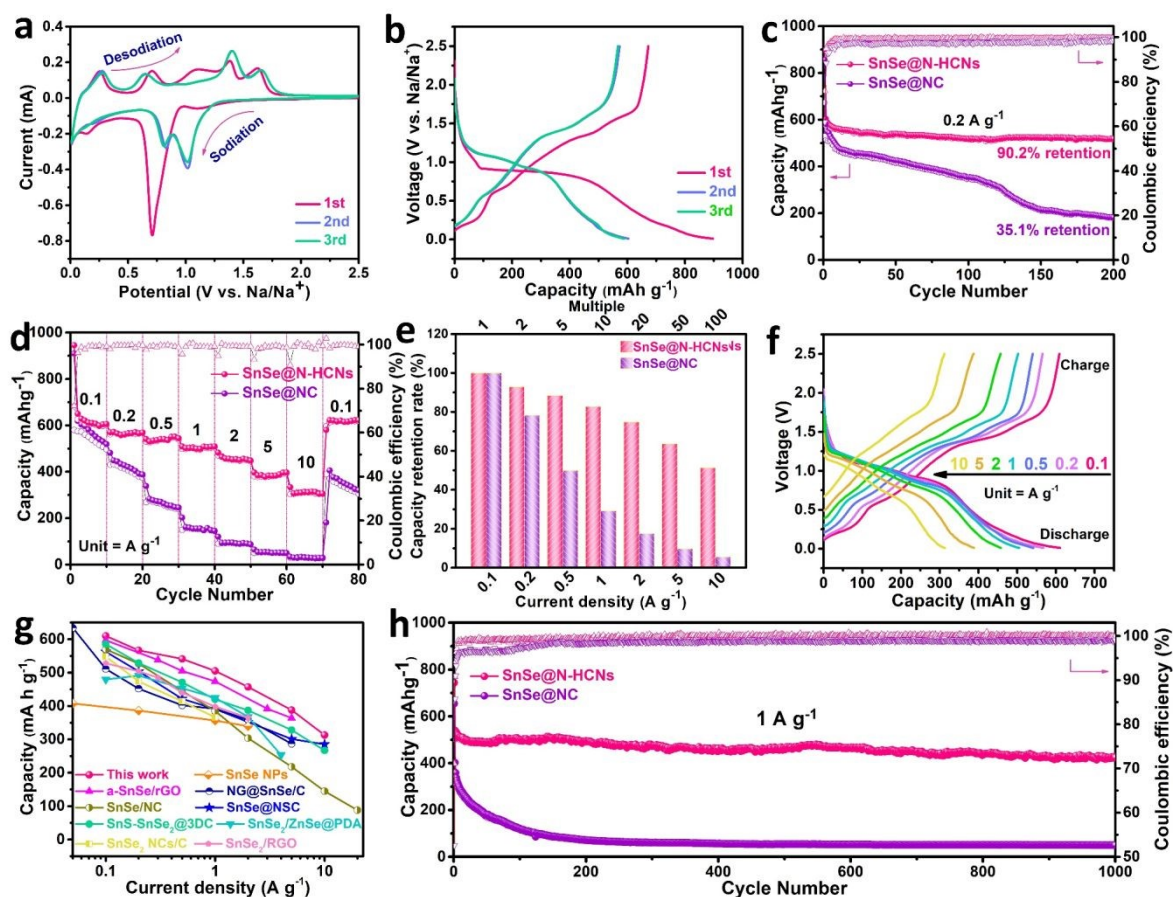
Figure 3. (a) Representative CV curves of the SnSe@N-HCNs electrode at a voltage range of 0.01-2.5 V and scan rate of 0.1 mV s^{-1}. (b) Charge-discharge voltage profiles of the SnSe@N-HCNs electrode at 0.2 A g^{-1}. (c) Cycling stability at 0.2 A g^{-1}, (d) rate abilities and (e) the capacity retention rate of the SnSe@N-HCNs and SnSe@NC. (e) The charge/discharge profiles of SnSe@N-HCNs at different current densities. (g) A comparison of the rate performance between SnSe@N-HCNs and recently reported tin selenides anode materials for SIBs. (h) Long-term cycling performance of the SnSe@N-HCNs and SnSe@NC at 1.0 A g^{-1}.
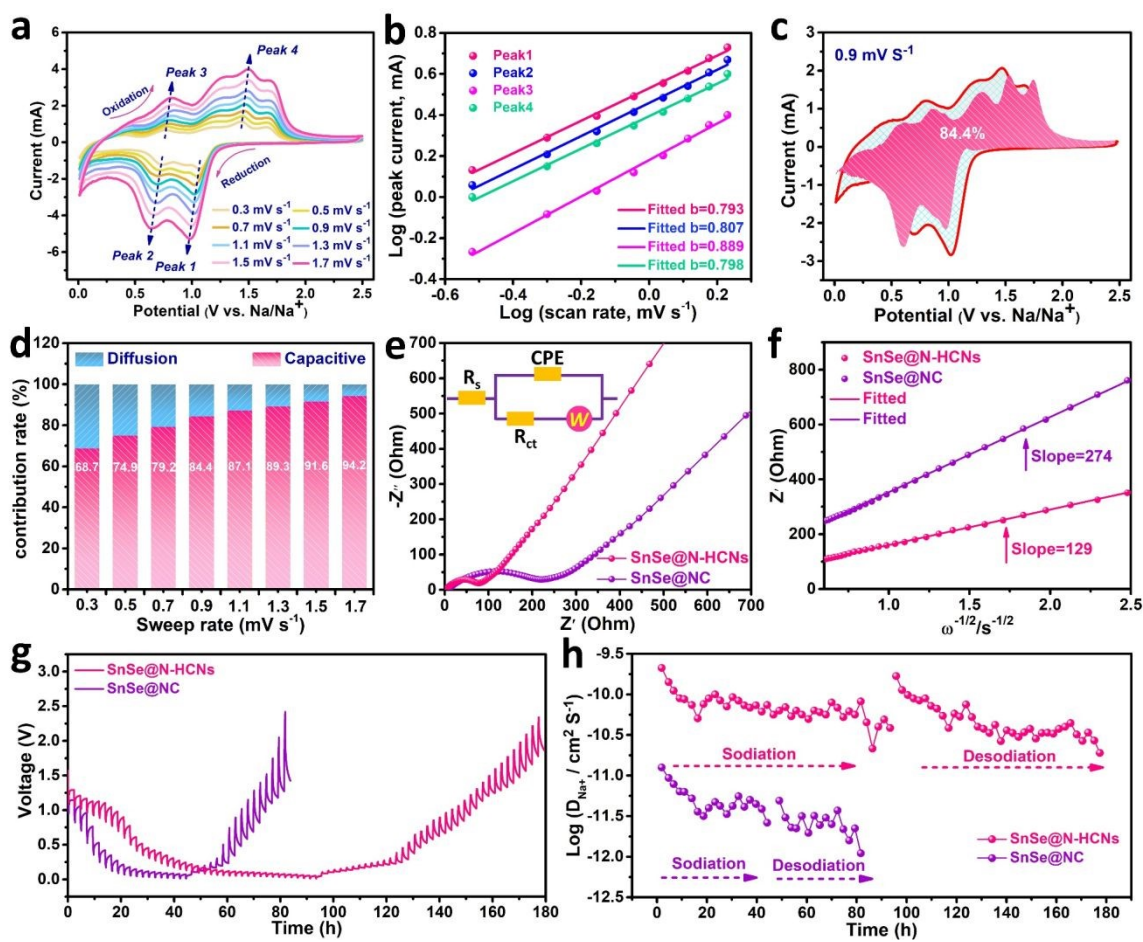
Figure 4. (a) CV curves at various scan rates from 0.3 to 1.7 mV s^{-1}, (b) linear relationships between logarithm currents and logarithm sweep rate, (c) capacitive contribution at 0.9 mV s^{-1}, (d) calculated capacitive contributions at different sweep rate for the SnSe@N-HCNs. (e) Nyquist plots and equivalent circuit (inset) used for the EIS analysis of the SnSe@N-HCNs and SnSe@NC at 0.2 A g^{-1} after 100 cycles. (f) linear fits of the Z` versus $\omega^{-1/2}$ ($\omega = 2\pi f$) in the low-frequency region. (g) GITT curves of SnSe@N-HCNs and SnSe@NC at 0.2 A g^{-1} after 100 cycles. (h) The Na-ion diffusion coefficient of SnSe@N-HCNs and SnSe@NC obtained via the GITT technique during sodiation and desodiation processes.
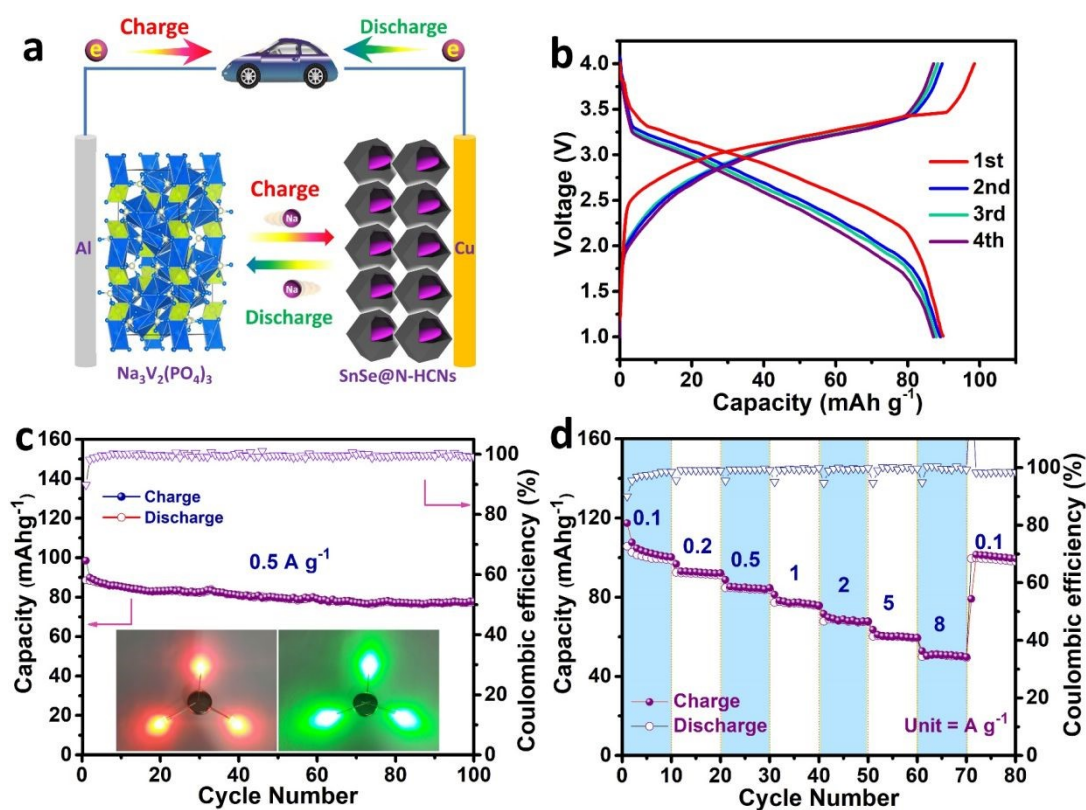
Figure 5. (a) Schematic illustration of the sodium-ion full battery with Na$_3$V$_2$(PO$_4$)$_3$/C//SnSe@N-HCNs couple. (b) Charge and discharge curves, (c) cycling stability at 0.5 A g^{-1} and (d) rate performance of the full battery. (Inset of c: photograph of different colors of LED lights powered by the full battery).